



Submitted: March 17, 2024

Revised: August 8, 2024

Accepted: September 10, 2024

Photoluminescent characteristics of solution-processed nanoscale copper oxide

S. Sachdeva , I. Choudhary 

Maharishi Markandeshwar (Deemed to be University), Mullana-Ambala, Haryana, India

 ishan.phy@gmail.com

ABSTRACT

In the present work, pure CuO nanoparticles were synthesized using the co-precipitation method, and their properties such as structural, morphological, and optical were elucidated. The obtained X-ray diffraction (XRD) patterns confirm that the synthesized CuO powders crystallize to a monoclinic phase. In addition to that, the appearance of the broad XRD peaks reflects the confinement of the particle size to nonorange. The average particle size of the synthesized CuO nanoparticles measured using field emission scanning electron microscopy (FESEM) image is 36.8 nm. Due to the size confinement to the nanoscale, the synthesized CuO nanoparticles showed a high optical band gap of 2.84 eV. Further, the emission properties of CuO measured using photoluminescence (PL) spectroscopy at an excitation wavelength of 300 nm reflects that most of the emission lies in the ultraviolet (UV) range. However, upon close investigation of the emission spectra, the peak corresponding to the blue emission was also observed. The appearance of this blue emission was the consequence of the various defects present in CuO such as oxygen vacancies and copper interstitials. The Commission Internationale de l'Eclairage (CIE) color coordinates for the blue color emitted by CuO nanoparticles is (0.15, 0.13), which lies close to the ideal blue color. Further, the synthesized CuO nanoparticles showed a high color purity of 84.71 % for blue color.

KEYWORDS

CuO • nanoparticles • absorption • emission • defects

Citation: Sachdeva S, Choudhary I. Photoluminescent characteristics of solution-processed nanoscale copper oxide. *Materials Physics and Mechanics*. 2024;52(6): 27–37.

http://dx.doi.org/10.18149/MPM.5262024_4

Introduction

In recent years, nanoscience and thin-film technology have led to the development of new technologically advanced devices. The major advantages of such devices include lightweight, non-toxic behavior, highly sensitive response, and high output performance with minimum losses [1]. Out of the various materials available, inorganic oxide semiconductors (IOS) are of great interest. IOS materials have a wide optical band gap range, large mobility values even in the amorphous phase, and serve as suitable host materials for various dopants [2–6]. Further, a notably enhanced performance of the devices has been observed for the devices fabricated using IOS nanostructures in comparison to their bulk counterparts. To date, due to the easy availability of the n-type metal oxide semiconductors such as zinc oxide (ZnO), titanium oxide (TiO₂), tin oxide (SnO₂), and tungsten oxide (WO₃), the nanostructures of n-type metal oxides semiconductors have been rigorously investigated worldwide. Numerous high-tech devices such as gas sensors [7–9], biosensors [10–12], nano thin film transistors [13–19], photovoltaic [20–23], and memory devices [24,25] have been reported in the literature based upon the n-type metal oxide semiconductors. Despite this most of the electronic industry

is still dominated by silicon (Si) based devices. This happens because of the availability of only a few p-type metal oxide semiconductors in nature. To fully replace the silicon (Si) based electronic industry with oxides-based electronics, it is essential to identify a suitable p-type inorganic metal oxide semiconductor that has comparable performance with n-type metal oxide semiconductors and can be processed by cost-effective means. Given this, recent studies have shown that oxides of copper possess inherent p-type semiconducting behavior due to the presence of negatively charged copper vacancies [26,27]. In addition to that, the oxides of copper showed a narrow optical band gap ranging from 1.2 eV to 2.3 eV, which can be easily tuned either by doping or synthesizing its nanostructures [28–31]. This makes the oxides of copper an ideal candidate for various optoelectronic devices such as solar cells, heterojunction diodes, and inverters.

In nature, the oxides of copper exist in two phases namely cuprous oxide (Cu_2O) and Cupric oxide (CuO). However, out of these, CuO has been reported to be the most stable form of copper oxide, since obtaining the Cu_2O phase requires a fine tunability of oxygen partial pressures [29,32]. In addition to that, the Cu_2O phase has a large probability of getting oxidized and converted into a much more stable CuO phase. However, in comparison to the n-type metal oxide semiconductors, the conductivity in the CuO is dominated by the hole conduction. Due to the presence of highly directional localized 2p orbitals from oxygen in valence band maximum (VBM) and deep-level traps near VBM, the hole mobility of CuO is hindered significantly [33,34]. Thus, a band gap modification might improve the performance of CuO . Since, the optical band gap of the semiconductor material depends upon the particle size, in this work, an attempt has been made *a)* to synthesize the nanoparticles of p-type CuO using a cost-effective, and low-temperature solution-based co-precipitation method, and *b)* to study the optical properties of CuO nanoparticles.

Materials and Methods

To prepare CuO nanoparticles, the solution-processed co-precipitation method was adopted. 0.01 moles of copper acetate monohydrate [$\text{Cu}(\text{CH}_3\text{COO})_2 \cdot \text{H}_2\text{O}$] from Sigma Aldrich with 99.9 % purity were mixed with 100 ml of laboratory absolute ethanol (99.9 % purity) in a round bottle flask. The flask was then subjected to an oil bath, which was well maintained at a temperature of 70 °C. The oil bath helps in maintaining a uniform and even temperature throughout the reaction. After a continuous vigorous stirring for 2 h, a transparent clear brown color solution with no segregation was obtained. At this point, 0.02 moles of sodium hydroxide (NaOH) were added to the reaction mixture. The addition of the NaOH increases the pH of the solution to 10.5, consequently, a co-precipitation reaction is forced and the solution turns slightly black in a few minutes indicating the formation of the pure copper oxide precipitates. The reaction mixture was then allowed to continuously stir for 2 h. The obtained precipitates were then separated from the solution using a centrifugation technique at 7000 rpm. However, the obtained precipitates were still wet and contained excess solvent. Hence, the obtained precipitates are placed in an oven for 4 h maintained at 100 °C. The dried precipitates were then ground in a mortar pastel and a fine black powder of CuO was obtained. The process flowchart of the synthesis has been presented in Fig. 1.

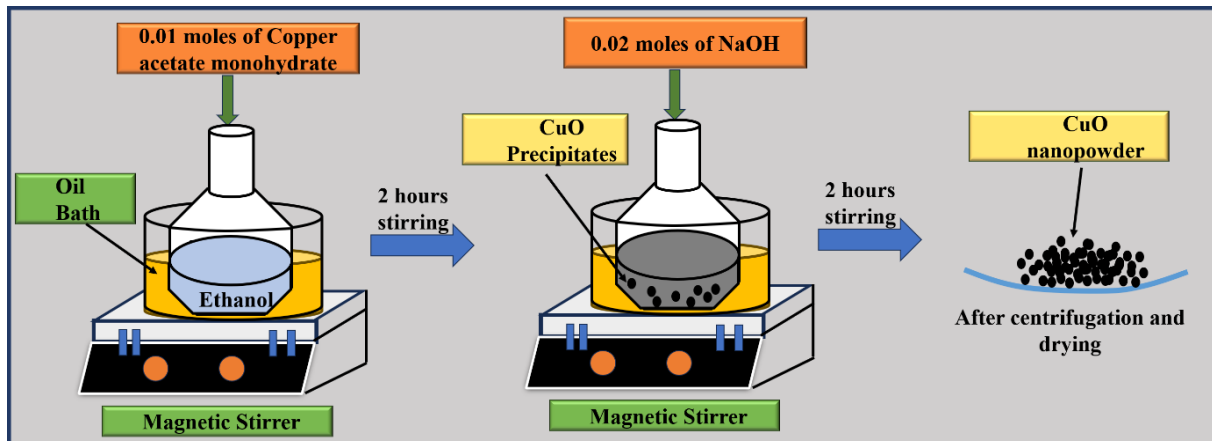


Fig. 1. Process flowchart of the CuO nanoparticles fabrication

Investigation of the structural, morphological, and optical properties of synthesized CuO powder was performed by various experimental techniques such as X-ray diffraction (XRD) (X'pert diffractometer of Philips), fourier infrared spectroscopy (FTIR) (Spectrum L1280130 FTIR spectrometer of Perkin Elmer), field emission scanning electron microscopy (FESEM), energy dispersive X-ray spectroscopy (EDS), UV visible spectroscopy (spectra max iD3), and spectrofluorophotometer (Shimadzu RF-5301PC) were used. To perform XRD measurements the synthesized CuO powder was spread on a glass plate and X-rays were incident on the sample at a grazing angle of 2° . The diffraction angle 2θ was varied from 20° to 80° with a step size of 0.02. For the study of optical properties, samples for UV visible and photoluminescence (PL) measurements were prepared by dispersing CuO powder in a pure ethanol solution, which was filled inside a 96-well plate. The 96-well plate was then implanted inside the UV-visible spectrophotometer to obtain the absorbance spectra.

Results and Discussion

Structural analysis

The XRD pattern of the synthesized CuO powder using the co-precipitation technique has been depicted in Fig. 2. Appearance of the strong diffraction peaks reveals that the synthesized CuO particles are crystalline. Peak matching performed using X'pert high score software confirms that the synthesized CuO powders have been crystallized to a monoclinic phase, which corresponds to JCPDS card No. 48-1548. The diffraction peaks located at a diffraction angle (2θ) equal to 32.08° , 35.60° , 38.47° , 48.16° , 53.80° , 57.71° , 61.19° , 65.30° , 67.52° , 72.34° , and 74.60° belong to the (110) , $\{(002), (11\bar{1})\}$, $\{(111), (200)\}$, $(20\bar{2})$, (020) , (202) , $(11\bar{3})$, $(31\bar{1})$, (113) , (331) , and (004) respectively.

Next, we analyse the appearance of broad XRD patterns obtained for the synthesized pure CuO. According to the literature, smaller crystallite size (D) and microstrain (ϵ) are the two factors that lead to the broadening of the XRD peaks [29].

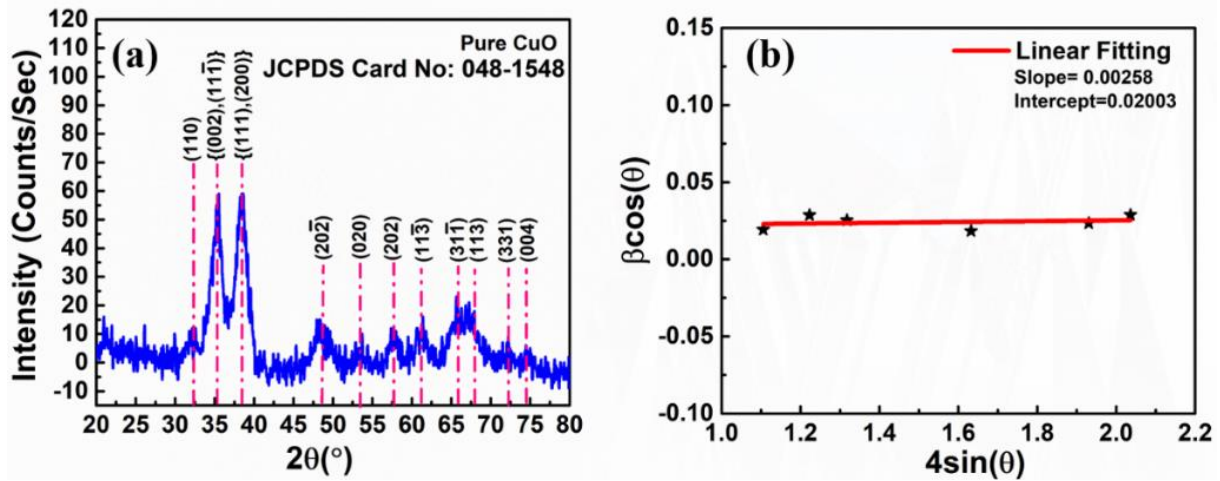


Fig. 2. (a) XRD pattern of synthesized pure CuO powder; (b) WHM plot of synthesized pure CuO

To quantify these factors simultaneously, the Williamson-Hall Method (WHM) can be adopted. According to this method, the total broadening of the XRD peak is given by: $(Broadening (\beta_T))_{(Total)} = (Broadening)_{(Size)} + (Broadening)_{(microstrain)}$, (1) where β_T represents the full width at half maximum (FWHM) of the corresponding XRD peak. The broadening due to the crystallite size can be quantified using the Scherer formula as:

$$\beta_{Crystallite\ size} = \frac{K\lambda}{D \cos\theta}, \quad (2)$$

where, K is shape factor, D is the crystallite size, λ is the X-ray wavelength, and θ is the diffraction angle. On the other hand, the microstrain broadening is quantified using:

$$\beta_{microstrain} = 4\varepsilon \cdot \tan \theta. \quad (3)$$

Upon substituting the Eqs. (2) and (3) in Eq. (1), a straight-line equation is obtained and is given as:

$$\beta_T \cos\theta = \varepsilon(4 \sin \theta) + \frac{K\lambda}{D}. \quad (4)$$

Hence, by plotting $\beta \cos\theta$ along Y-axis and $4 \sin \theta$ along X-axis, the average values of crystallite size and the microstrain can be obtained. The value of the microstrain is governed by the slope of the curve, while the intercept governs the crystallite size. Figure 2(b) represents the corresponding WHM plot for the synthesized pure CuO powder. Thus, the calculated value of the microstrain is 0.00258 and the average crystallite size of the synthesized pure CuO powder is around 6.83 nm.

Next, we determine the lattice parameters and lattice volume of the CuO unit cell. For a monoclinic lattice the d-spacing is given by

$$\frac{1}{d^2} = \frac{1}{\sin^2\beta} \left[\frac{h^2}{a^2} + \frac{k^2 \sin^2\beta}{b^2} + \frac{l^2}{c^2} - \frac{2hl \cos\beta}{ac} \right], \quad (5)$$

where h, k, l are Miller indices of the plane, d is an interplanar spacing, a, b, c are lattice constants and β is the angle greater than 90° . The values of $\beta, a, b,$ and c are calculated by considering (200), (002), (202), ($20\bar{2}$) and (020) lattice planes. The lattice volume of the monoclinic lattice then can be calculated using

$$V = abc \cdot \sin\beta. \quad (6)$$

All the lattice parameters and lattice volume has been listed in Table 1.

Table 1. Lattice parameters of synthesized pure CuO nanoparticles

Lattice Plane	d-spacing	β , °	Lattice constant a , Å	Lattice constant b , Å	Lattice constant c , Å	Lattice volume, Å ³
(200)	2.3080	99.44	4.6794	3.4124	5.0817	80.0446
(002)	2.5064					
(202)	1.5770					
(20 $\bar{2}$)	1.8599					
(020)	1.7062					

Morphological analysis: FESEM and EDS

The FESEM image of the synthesized pure CuO nanoparticles at a magnification of 30000x is shown in Fig. 3(a). The CuO nanoparticles showed an agglomerated spherical shape morphology. To determine the particle size using FESEM, the particle size of various nanoparticles distributed in the FESEM image was calculated with the help of Image-J software. The obtained data has been represented in Fig. 3(b) as a histogram. Using a normal distribution the calculated mean particle size of the synthesized CuO nanoparticles is 36.8 nm, with a standard deviation of 16.71 nm. The obtained result is also consistent with the crystallite size calculated using the XRD data.

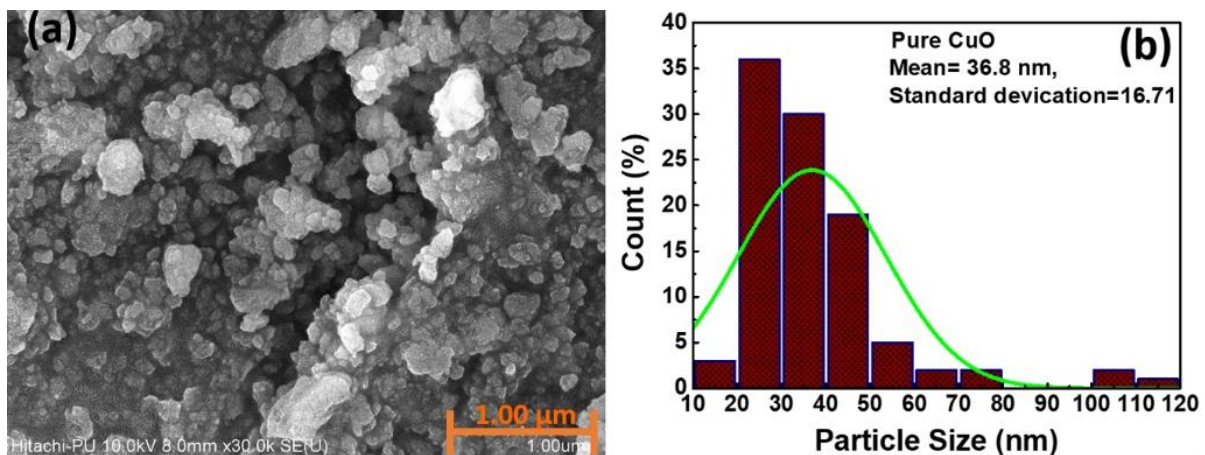


Fig. 3. (a) FESEM image of CuO nanoparticles at a magnification of 30000x; (b) histogram and normal distribution of the CuO nanoparticles particle size

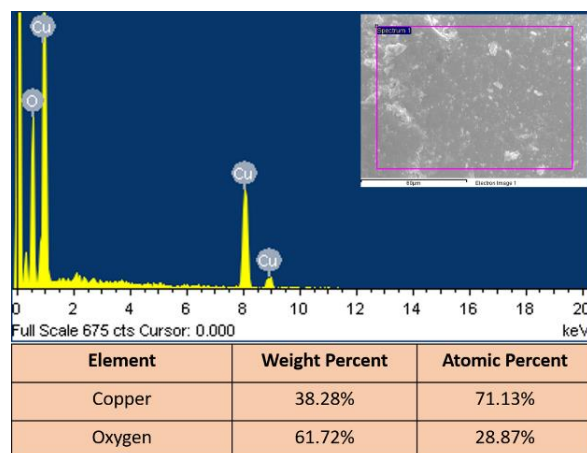


Fig. 4. EDS spectra of synthesized CuO nanoparticles

Next, we determine the elemental composition of the synthesized pure CuO nanoparticles using EDS spectroscopy, as shown in Fig. 4. The EDS spectra clearly show the peaks of copper (Cu) and oxygen (O), indicating the presence of both Cu and O ions.

The corresponding atomic percentages of Cu and O in synthesized CuO nanoparticles are 71.13 and 28.87 %, respectively. In terms of weight percentage, the Cu ion has 38.28 wt. %, and the O ion has a 61.72 wt. %.

Chemical Analysis

To identify the presence of various functional groups, stretching, and vibration modes present in the synthesized CuO nanoparticles, FTIR spectroscopy is performed. The obtained FTIR spectra have been presented in Fig. 5. According to the previous reports the peaks corresponding to the vibration and stretching of the CuO phase are located from 400 to 900 cm^{-1} band [35]. The obtained peak centred at 476.86 cm^{-1} corresponds to the A_1 mode of vibration and is due to the stretching of Cu-O along [101] direction [36]. Further, the peaks at 745.46 and 856.01 cm^{-1} are associated with the Cu-O stretching mode along $[\bar{2}02]$ direction [29]. In addition to that, the absence of any extra peak in the range of 600 to 650 cm^{-1} indicates the absence of IR active modes of the Cu_2O phase [36]. This eliminates the possibility of the formation of the secondary Cu_2O phase or complexes.

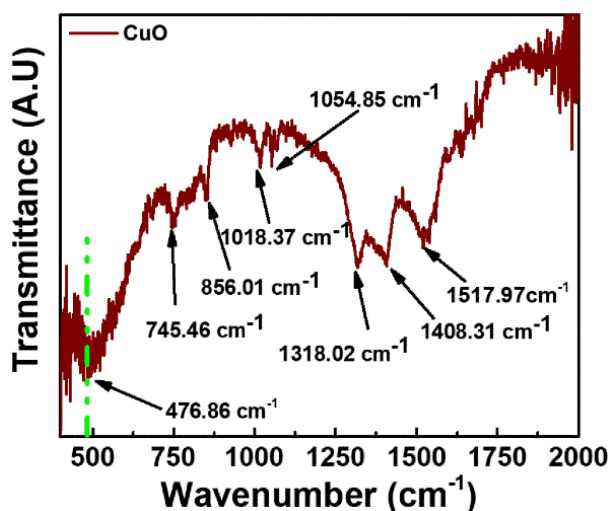


Fig. 5. FTIR spectra of synthesized CuO nanoparticles

The FTIR peaks that appear above 900 cm^{-1} are due to the presence of the functional groups attached to the CuO nanoparticles. The peaks appeared at 1318.02, 1408.31, and 1517.97 cm^{-1} are associated with the presence of cis-di substituted alkenes and amide (COO^-) groups [29,37]. The peaks at 1018.37 and 1054.85 cm^{-1} are associated with the O-H bond stretching of the alkyl group [34,38].

Absorption properties

Figure 6(a) represents the absorption spectra of the synthesized pure CuO nanoparticles. The obtained spectra depict that pure CuO nanoparticles have an absorption edge located at 300.6 nm.

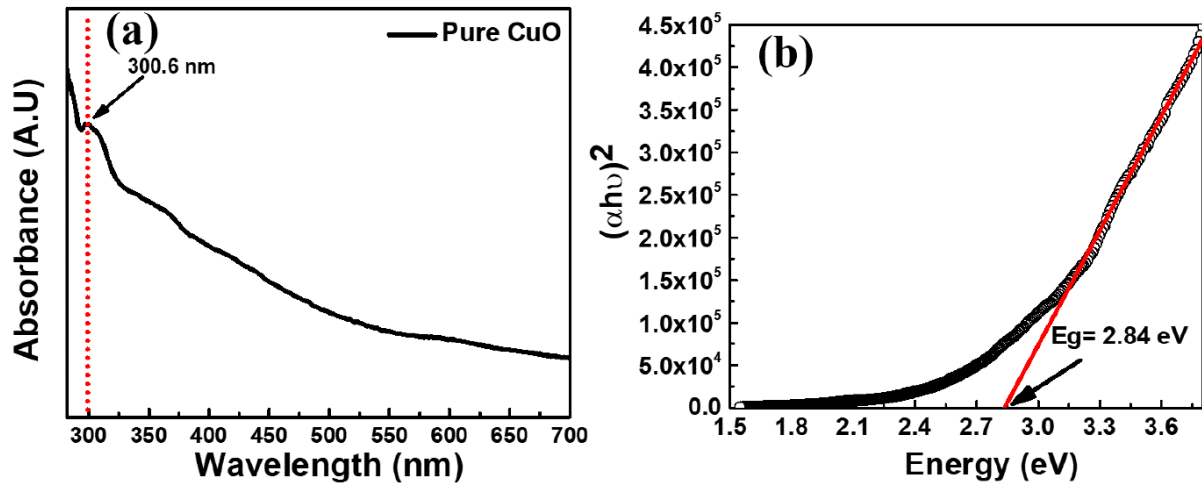


Fig. 6. (a) UV absorption spectra of synthesized pure CuO nanoparticles; (b) the $(\alpha h\nu)^2$ vs $h\nu$ plot for synthesized pure CuO nanoparticles

To determine the optical band gap of the pure CuO, the well-known Tauc's method was adopted [39,40]. According to this method, the absorption coefficient α for a material can be given as:

$$\alpha h\nu = A(h\nu - E_g)^n, \quad (7)$$

where α represents the absorption coefficient, E_g represents the optical band gap, A is a constant, and exponent n can have values 0.5, 1.5, 2, or 3. The value of n determines the type of electronic transitions. In the case of direct electronic transitions, the value of n is equal to 0.5. The CuO is also a direct band gap semiconductor [41], hence we take $n = 0.5$ in our case also.

Figure 6(b) represents the $(\alpha h\nu)^2$ vs $h\nu$ plot for synthesized pure CuO nanoparticles. The optical band gap of 2.84 eV is determined using this approach for pure CuO nanoparticles. The obtained optical gap of synthesized pure CuO nanoparticles is quite higher in comparison to the bulk CuO, which is 1.2-1.9 eV [42]. This increase in the optical band gap might be due to the lower crystallite size of synthesized CuO nanoparticles. At the nanoscale level, the crystallite size becomes smaller than the Bohr radius of the exciton due to which the discrete energy level forms at the edges of the conduction and valence conduction band. Consequently, the band gap increases.

Emission properties

Figure 7(a,b) represents the PL spectra of the CuO nanoparticles at an excitation wavelength of 300 nm. The pure CuO nanoparticles showed a broad emission spectrum spreading from 320 to 600 nm.

To locate the exact peak positions, first, we removed the background using the b-spline interpolation method in Origin 9.0 software. The obtained emission spectra curve is then fitted using the Voigt function fitting. The Voigt function is a mixture of Gauss and Lorentz functions. According to the fitted curve the obtained emission spectra consists of 2 major emissions peaks positioned at 387.24 and 454.92 nm. The emission peak at 387.24 nm lies in the ultraviolet region and is of no interest. On the other hand, the emission peak at 454.92 nm corresponds to the blue region of the visible spectra, which is confirmed by plotting an XY chromaticity coordinate graph with the help of the

standard Commission Internationale de l'Éclairage (CIE) diagram, as depicted in Fig. 8. GOCIE software is used to prepare the CIE diagram. The obtained color coordinates corresponding to the emission wavelengths of 454.90 nm are (0.15; 0.13) and are marked as a black circle in Fig. 8.

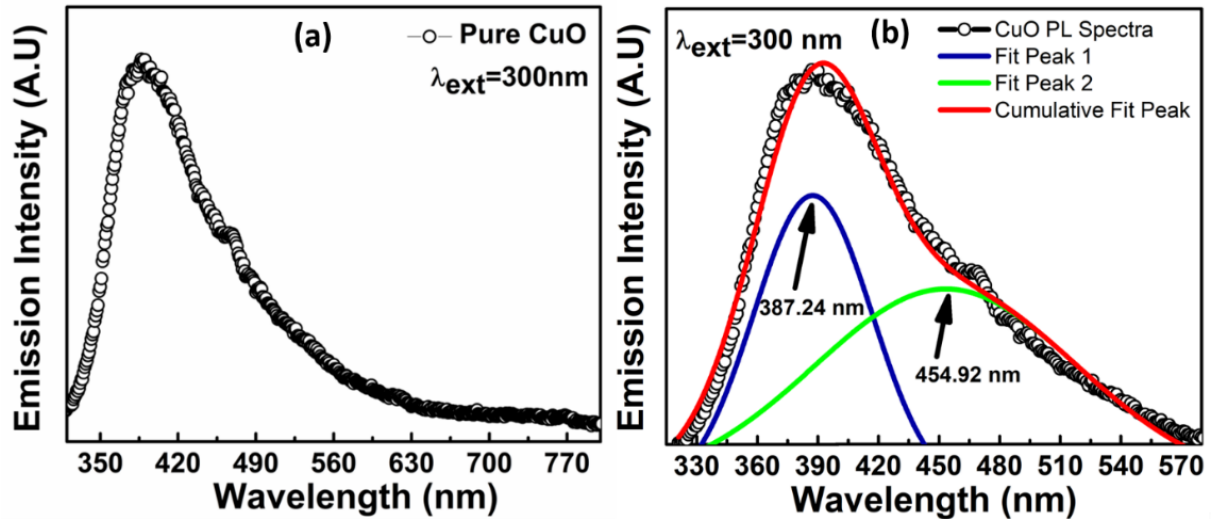


Fig. 7. (a) PL spectra of synthesized CuO nanoparticles at an excitation wavelength of 300 nm; (b) curve fitting of the emission peaks of synthesized CuO nanoparticles

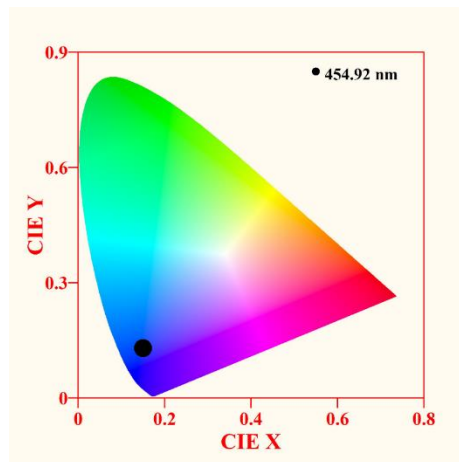


Fig. 8. CIE diagram of CuO nanoparticles at an excitation wavelength of 300 nm

Table 2. Defect reaction in synthesized CuO nanoparticles

$0.5O_2 \leftrightarrow \dot{V}_O + 2e^-$	Formation of oxygen vacancies
$Cu_{Cu}^x \leftrightarrow V_{Cu}'' + \dot{C}u_i$	Formation of negatively charged copper vacancies and copper interstitials

The emission peak at 387.24 nm appears due to the electron-hole pair recombination in free excitons. Since this peak lie in the UV region, it is of no interest. On the other hand, the emission peak centred at 454.92 nm lies in the blue region of the visible spectra. This blue emission peak is attributed to the defects present in the copper oxide such as surface states, oxygen vacancies, copper vacancies, and interstitial defects.

According to the reports of El-Trass et al. [43] the emission peak at 454.92 nm corresponds to the copper interstitial and oxygen vacancies. The corresponding Kroger-Vink defect reactions for the formation of these defects in CuO have been listed in Table 2.

Next, we determine the color purity of the blue colour emission corresponding to the emission wavelength of 454.92 nm using the expression:

$$\text{Color purity} = \frac{\sqrt{(Z_S - Z_I)^2 + (Y_S - Y_I)^2}}{\sqrt{(Z_D - Z_I)^2 + (Y_D - Y_I)^2}} \times 100\%, \quad (8)$$

where, $(Z_I; Y_I)$, $(Z_S; Y_S)$, and $(Z_D; Y_D)$ are the color coordinates of the standard illuminate point (0.3101; 0.3162), sample, and respective ideal blue color (0.14; 0.08). The calculated value of the color purity for the synthesized CuO nanoparticles is found to be 84.71 %.

In summary, it is established that synthesized CuO nanoparticles mostly emit in the UV range. However, the emission spectra also consist of the peak corresponding to the blue emission, which appeared due to the formation of oxygen vacancies and copper interstitial defects.

Conclusions

Pure CuO nanoparticles are synthesized using the co-precipitation method. The Broad XRD peaks suggest the particle size lies in the nano range and is confirmed using FESEM. The average particle size of the synthesized CuO nanoparticles is 36.8 nm. The synthesized CuO nanoparticles showed a high band gap of 2.84 eV due to the quantum size effect. Further, Blue emission from pure CuO nanoparticles at an excitation wavelength of 300 nm is demonstrated. The presence of the various defects in CuO such as oxygen vacancies and copper interstitials are the responsible factors for the appearance of this blue emission. The obtained CIE color co-ordinates for the blue color is (0.15, 0.13), and lies close to the ideal blue color co-ordinates (0.14, 0.08). Further, the synthesized CuO nanoparticles showed a high colour purity of 84.71 %.

References

1. Yu X, Marks TJ, Facchetti A. Metal oxides for optoelectronic applications. *Nat Mater*. 2016;15: 383–396.
2. Grundmann M, Klüpfel F, Karsthof R, Schlupp P, Schein FL, Splith D, Yang C, Bitter S, Wenckstern H. Oxide bipolar electronics: materials, devices and circuits. *Journal of Physics D: Applied Physics*. 2016;49(21): 213001.
3. Martins RFP, Ahnood A, Correia N, Pereira LMNP, Barros R, Barquinha PMCB, Costa R, Ferreira IMM, Nathan A, Fortunato EEMC. Recyclable, Flexible, Low-Power Oxide Electronics. *Advanced Functional Materials*. 2013;23: 2153–2161.
4. Petti L, Munzenrieder N, Vogt C, Faber H, Büthe L, Cantarella G, Bottacchi F, Anthopoulos TD, Tröster G. Metal oxide semiconductor thin-film transistors for flexible electronics. *Appl Phys Rev*. 2016; 3(2): 021303.
5. Hosono H, Yasukawa M, Kawazoe H. Novel oxide amorphous semiconductors: transparent conducting amorphous oxides. *Journal of Non-Crystalline Solids*. 1996;203: 334–344.
6. Hosono H, Kikuchi N, Ueda N, Kawazoe H. Working hypothesis to explore novel wide band gap electrically conducting amorphous oxides and examples. *Journal of Non-Crystalline Solids*. 1996;198–200(1): 165–169.
7. Nie L, Guo X, Gao C, Wu X, Chen J, Peng L. Fabrication and optical hydrogen gas sensing property of hierarchical WO₃ Porous/Nanowires film. *Materials Letters*. 2022;314: 131805.
8. Franco MA, Conti PP, Andre RS, Correa DS. A review on chemiresistive ZnO gas sensors. *Sensors and Actuators Reports*. 2022;4: 100100.
9. Tian X, Cui X, Lai T, Ren J, Yang Z, Xiao M, Wang B, Xiao X, Wang Y. Gas sensors based on TiO₂ nanostructured materials for the detection of hazardous gases: A review. *Nano Materials Science*. 2021;3(4): 390–403.

10. Rafiee Z, Mosahebfard A, Sheikhi MH. High-performance ZnO nanowires-based glucose biosensor modified by graphene nanoplates. *Materials Science in Semiconductor Processing*. 2020;115: 105116.
11. Shetti NP, Bukkitgar SD, Reddy KR, Reddy CV, Aminabhavi TM. ZnO-based nanostructured electrodes for electrochemical sensors and biosensors in biomedical applications. *Biosensors and Bioelectronics*. 2019;141: 111417.
12. Pillai RR, Sreelekshmi PB, Meera AP. Enhanced biological performance of green synthesized copper oxide nanoparticles using Pimenta dioica leaf extract. *Materials Today: Proceedings*. 2022;50(2): 163–172.
13. Choudhary I, Deepak. Study on dielectric properties of PVP and Al₂O₃ thin films and their implementation in low-temperature solution-processed IGZO-based thin-film transistors. *Journal of Materials Science: Materials in Electronics*. 2021;32: 7875–7888.
14. Zhang L, Wei J, Zhou K, Wan C, Sun H. Highly transparent IGZO-TFTs uses IGZO source and drain electrodes with a composite insulation layer structure. *Optik*. 2020;204: 163654.
15. Kang M-S, Cho W-J. High-performance amorphous indium gallium zinc oxide thin-film transistors with sol-gel processed gate dielectric and channel layer fabricated using microwave irradiation. *Current Applied Physics*. 2018;18(9): 1080–1086.
16. Xue J, Song J, Dong Y, Xu L, Li J, Zeng H. Nanowire-based transparent conductors for flexible electronics and optoelectronics. *Science Bulletin*. 2017;62(2): 143–156.
17. Park S, Kim C-H, Lee W-J, Sung S, Yoon M-H. Sol-gel metal oxide dielectrics for all-solution-processed electronics. *Materials Science and Engineering: R: Reports*. 2017;114: 1–22.
18. Yu X, Marks TJ, Facchetti A. Metal oxides for optoelectronic applications. *Nature Materials*. 2016;15: 383–396.
19. Lorenz M, Ramachandra Rao MS, Venkatesan T, Fortunato E, Barquinha P, Branquinho R, Salgueiro D, Martins R, Carlos E, Liu A, Shan FK, Grundmann M, Boschker H, Mukherjee J, Priyadarshini M, DasGupta N, Rogers DJ, Teherani FH, Sandana EV, Bove P, Rietwyk K, Zaban A, Veziridis A, Weidenkaff A, Muralidhar M, Murakami M, Abel S, Fompeyrine J, Zuniga-Perez J, Ramesh R, Spaldin NA, Ostanin S, Borisov V, Mertig I, Lazenka V, Srinivasan G, Prellier W, Uchida M, Kawasaki M, Pentcheva R, Gegenwart P, Miletto Granozio F, Fontcuberta J, Pryds N. The 2016 oxide electronic materials and oxide interfaces roadmap. *Journal of Physics D: Applied Physics*. 2016;49: 433001.
20. Roa S, Sandoval M, Burgos MJC, Manidurai P, Suárez S. Potential photovoltaic properties of thin film solar cells based on chemically deposited ZnO/PbSe junctions. *Journal of Alloys and Compounds*. 2021;871: 159559.
21. Saleh Al-Khazali SM, Al-Salman HS, Hmood A. Low cost flexible ultraviolet photodetector based on ZnO nanorods prepared using chemical bath deposition. *Materials Letters*. 2020;277: 128177.
22. Aboulouard A, Gultekin B, Can M, Erol M, Jouaiti A, Elhadadi B, Zafer C, Demic S. Dye sensitized solar cells based on titanium dioxide nanoparticles synthesized by flame spray pyrolysis and hydrothermal sol-gel methods: a comparative study on photovoltaic performances. *Journal of Materials Research and Technology*. 2020;9(2): 1569–1577.
23. Kumar Rana A, Ban D-K, Patel M, Yun J-H, Kim J. A transparent photovoltaic device based on Cu₂O/ZnO/AZO for see-through applications. *Materials Letters*. 2019;255: 126517.
24. Hu L, Gao W, Xiao M, Li Z. Interfacial reaction induced digital-to-analog resistive switching in TiO₂-based memory devices. *Physica B: Condensed Matter*. 2022;632: 413730.
25. Yu Z, Sun T, Liu B, Zhang L, Chen H, Fan X, Sun Z. Self-rectifying and forming-free nonvolatile memory behavior in single-crystal TiO₂ nanowire memory device. *Journal of Alloys and Compounds*. 2021;858: 157749.
26. Meyer BK, Polity A, Reppin D, Becker M, Hering P, Klar PJ, Sander T, Reindl C, Benz J, Eickhoff M, Heiliger C, Heinemann M, Blasing J, Krost A, Shokovets S, Muller C, Ronning C. Binary copper oxide semiconductors: From materials towards devices. *Phys. Status Solidi B*. 2012;249(8): 1487–1509.
27. Li J, Tokumitsu E, Koyano M, Mitani T, Shimoda T. Highly conductive p-type amorphous oxides from low-temperature solution processing. *Applied Physics Letters*. 2012;101(13): 132104.
28. Usha V, Kalyanaraman S, Thangavel R, Vettumperumal R. Effect of catalysts on the synthesis of CuO nanoparticles: Structural and optical properties by sol-gel method. *Superlattices and Microstructures*. 2015;86: 203–210.
29. Kumar N, Parui SS, Limbu S, Mahato DK, Tiwari N, Chauhan RN. Structural and optical properties of sol-gel derived CuO and Cu₂O nanoparticles. *Materials Today: Proceedings*. 2021;41(2): 237–241.
30. Selvaraj SP. Enhanced surface morphology of copper oxide (CuO) nanoparticles and its antibacterial activities. *Materials Today: Proceedings*. 2022;50(7): 2865–2868.

31. Sivayogam D, Kartharinal Punithavathy I, Johnson Jayakumar S, Mahendran N. Study on structural, electro-optical and optoelectronics properties of CuO nanoparticles synthesis via sol gel method. *Materials Today: Proceedings*. 2022;48(2): 508–513.
32. Paul CA, Ranjith Kumar E, Suryakanth J, Abd El-Rehim AF. Analysis and characterization of structural, morphological, thermal properties and colloidal stability of CuO nanoparticles for various natural fuels. *Ceramics International*. 2023;49(19): 31193–31209.
33. Li BS, Akimoto K, Shen A. Growth of Cu₂O thin films with high hole mobility by introducing a low-temperature buffer layer. *J Cryst Growth*. 2009;311(4): 1102–1105.
34. Ghotbi MY, Rahmati Z. Nanostructured copper and copper oxide thin films fabricated by hydrothermal treatment of copper hydroxide nitrate. *Materials & Design*. 2015;85: 719–723.
35. Ethiraj AS, Kang DJ. Synthesis and characterization of CuO nanowires by a simple wet chemical method. *Nanoscale Research Letters*. 2012;7: 70.
36. Singh SJ, Chinnamuthu P. Highly efficient natural-sunlight-driven photodegradation of organic dyes with combustion derived Ce-doped CuO nanoparticles. *Colloids and Surfaces A: Physicochemical and Engineering Aspects*. 2021;625: 126864.
37. Choudhary I, Shukla R, Sharma A, Raina KK. Effect of excitation wavelength and europium doping on the optical properties of nanoscale zinc oxide. *Journal of Materials Science: Materials in Electronics*. 2020;31: 20033–20042.
38. Albert Manoharan A, Chandramohan R, David prabu R, Valanarasu S, Ganesh V, Shkir M, Kathalingam A, AlFaify S. Facile synthesis and characterization of undoped, Mn doped and Nd co-doped CuO nanoparticles for optoelectronic and magnetic applications. *Journal of Molecular Structure*. 2018;1171: 388–395.
39. Choudhary I, Sehrawat R, Mehta S, Mittal R, Dhawan R, Rana K, Suraj, Sachdeva S. Photoluminescent and magnetic characteristics of cobalt and manganese doped nanoscale zinc oxide. *Journal of Materials Science: Materials in Electronics*. 2023;34: 1505.
40. Tauc J. Optical properties and electronic structure of amorphous Ge and Si. *Materials Research Bulletin*. 1968;3(1): 37–46.
41. Dhineshbabu NR, Rajendran V, Nithyavathy N, Vetumperumal R. Study of structural and optical properties of cupric oxide nanoparticles. *Applied Nanoscience*. 2016;6: 933–939.
42. Xu L, Zheng G, Pei S, Wang J. Investigation of optical bandgap variation and photoluminescence behavior in nanocrystalline CuO thin films. *Optik*. 2018;158: 382–390.
43. El-Trass A, ElShamy H, El-Mehasseb I, El-Kemary M. CuO nanoparticles: Synthesis, characterization, optical properties and interaction with amino acids. *Applied Surface Science*. 2012;258(7): 2997–3001.

About Authors

Shubham Sachdeva  

M. Sc., Research Scholar (Maharishi Markandeshwar (Deemed to be University), Mullana-Ambala, Haryana, India)

Ishan Choudhary  

PhD, Assistant Professor (Maharishi Markandeshwar (Deemed to be University), Mullana-Ambala, Haryana, India)